Chinese Chemical Letters 37 (2026) 111563

Contents lists available at ScienceDirect

Chinese Chemical Letters

journal homepage: www.elsevier.com/locate/cclet

Aluminate-mediated assembly of Keggin-type thorium-oxo clusters with a substitutable central octahedron and tunable shell ligands

Chunhui Wang[a], Zhe Han[a], Yuan Gao[a], Chaoyue Fan[a], Puyong He[a], Bojun Li[a], Dong Ma[a], Yang Zhang[a], Lei Zhang[b], Jie Qiu[a,*]

[a] School of Energy and Power Engineering, Xi'an Jiaotong University, Xi'an 710049, China
[b] Ningbo Institute of Materials Technology and Engineering, Chinese Academy of Sciences, Ningbo 315201, China

ARTICLE INFO

Article history:
Received 26 May 2025
Revised 2 July 2025
Accepted 8 July 2025
Available online 8 July 2025

Keywords:
Metal-oxo cluster
Keggin-type architecture
Thorium-oxo cluster
Self-assembly
Hydrolysis
Heterometallic ions

ABSTRACT

Metal-oxo clusters (MOCs), particularly those with renowned Keggin-type architecture, have been extensively studied for their facile synthesis, robust stability, and diverse applications. However, the isolation of thorium-oxo clusters with novel structural motifs remains elusive due to the distinctive hydrolytic behaviour of Th^{4+} ions. Herein, we report nine electropositive α-Keggin-type thorium-oxo clusters, $M@Th_{12}@L_8$ (where M is fully or co-occupied by Al^{3+}, W^{6+}, Mo^{6+}, V^{5+}, Cr^{3+}, or Mn^{4+}; L = Al or Ga), synthesized *via* aluminate-regulated Th^{4+} hydrolysis. Unlike $Th_6(O/OH)_8$-based structures for most reported thorium-oxo clusters, $M@Th_{12}@L_8$ features an unprecedented triple-layered Platonic architecture: a central MO_6 octahedron, a Th_{12} icosahedron, and an outer cube of eight LO_5 ligands. Structural rigidity maintains invariant M–O bond lengths despite variable MO_6 and LO_5 units, while the central M ion dictates solution pH during cluster formation, crystallization kinetics, crystal yield, and tunable optical properties. Time-resolved small-angle X-ray scattering (SAXS) and ^{27}Al magic-angle spinning (MAS) nuclear magnetic resonance (NMR) unveil the partial decomposition of aluminate precursors and the synchronized self-assembly of $M@Th_{12}@L_8$. This work advances our understanding of thorium hydrolysis in heterometallic systems and establishes a modular strategy to prepare MOCs with tailored architectures and functionalities.

© 2026 Published by Elsevier B.V. on behalf of Chinese Chemical Society and Institute of Materia Medica, Chinese Academy of Medical Sciences.

Since their initial discovery by Berzelius in 1826 [1], Keggin-type metal-oxo clusters and related materials have attracted considerable interest due to their convenient synthetic methods, remarkable chemical stability, and versatile applications in many fields such as catalysis, energy storage and conversion, biomedicine, and materials science [2–5]. The classical Keggin cluster contains a central XO_4 (X = P, Si, Ge, As, *etc.*) tetrahedron surrounded by twelve MO_6 octahedra (M = W and Mo) [6]. Recent advances in synthetic chemistry have propelled the exploration of Keggin-type clusters beyond traditional confines, extending to main group metals (Al_{13} [7]), other transition metals (Fe_{13} [8], Mn_{13} [9], Zr_{13} [10], and Hf_{13} [11]), and lanthanides (Eu_{13} [12]). However, Keggin-type actinide-oxo clusters remain largely unexplored.

Research on actinide-oxo clusters lags far behind other metals' clusters, primarily due to the radioactivity and complex chemical behaviors of actinides [13]. Among actinides, thorium is particularly noteworthy as the most abundant in Earth's crust [14] and the fuel for thorium nuclear reactors [15]. Therefore, a thorough understanding of thorium chemistry is crucial for its practical applications and addressing associated challenges, including mineral extraction, nuclear fuel preparation, radioactive waste processing, and the decorporation of internalized radionuclides [15–17]. The most common oxidation state of thorium is +4. Owing to the relatively high charge and small radius, Th^{4+} ions readily undergo hydrolysis and condensation at pH > 2, forming various products such as monomers, oligomers, colloids, and precipitates [18]. When suitable ligands are present to coordinate with thorium ions on the surface of hydrolysis products, thorium-oxo clusters form [19]. The presence of these hydrolysis products can not only complicate thorium extraction but also impact its solubility and migration in the natural environment [20]. Despite its significance, research on thorium-oxo clusters remains limited compared to non-radioactive metals or even more radioactive neptunium and plutonium [21–24].

To date, only a few dozen thorium-oxo clusters have been reported [19,25–34]. The most common are hexanuclear clusters

* Corresponding author.
E-mail address: qiujie1228@xjtu.edu.cn (J. Qiu).

https://doi.org/10.1016/j.cclet.2025.111563
1001-8417/© 2026 Published by Elsevier B.V. on behalf of Chinese Chemical Society and Institute of Materia Medica, Chinese Academy of Medical Sciences.

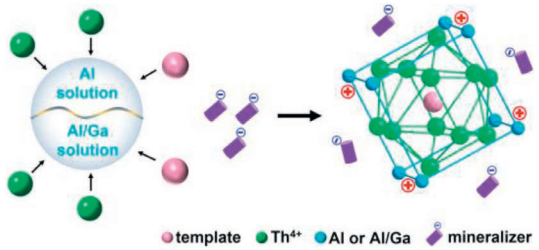
with octahedral $Th_6(O/OH)_8$ cores stabilized by various ligands [19,25–29,34], while the largest cluster identified is a dodecamer (Th_{12}) formed by linking two $Th_6(O/OH)_8$ subunits [33]. In contrast, other tetravalent metal-oxo clusters exhibit greater diversity and higher nuclearity. For example, the highest nuclearity clusters reported for Zr^{4+}, Ce^{4+}, U^{4+}, Np^{4+}, and Pu^{4+} are Zr_{70} [21], Ce_{100} [22], U_{84} [35], Np_{38} [24], and Pu_{38} [23], respectively. The isolation of thorium-oxo clusters with higher nuclearity or novel topological architectures remains challenging. This difficulty primarily stems from the distinctive hydrolytic property and reactivity of Th^{4+} ions compared to other tetravalent metal ions [36,37]. To address this challenge, it is crucial to explore and regulate the hydrolysis behaviors of Th^{4+} ions.

The majority of reported thorium-oxo clusters have been synthesized by controlling thorium hydrolysis through adjusting the solution pH, reaction temperature, solvents, and ligands [19,25–34]. Beyond these conventional approaches, studies of transition metal and lanthanide clusters have widely applied the method by introducing heterometallic ions into the synthesis, yielding mixed-metal clusters with more diverse structures, richer properties, and broader applications [38,39]. In contrast, thorium-containing mixed-metal oxo clusters remain limited. Beyond several clusters that were synthesized using lacunary polyoxometalates (POMs) of W and Mo to stabilize thorium ions [40], the known heterometallic thorium-oxo clusters are only a few, mainly including $Th_2Al_6(edta)_2$ [41], $Th_2Al_6(hedta)_2$ [42], $Th_2Al_8(hdpta)$ [42], $Th_2Al_8(heidi)$ [43], $Th_4Al_{10}(edta)$ [41], $ThFe_2(dhpta)$ [43], $Th_2Fe_2(cit)$ [43], $Th_2Fe_{10}(PhPO_3)$ [44], $Th_6Mn_{10}(PhCOO)$ [45], $Th_9Ag_6(PyCOO)$ [46], and $Th_9Ag_{12}(PyCOO)$ [46]. These clusters form through the synergistic effects of heterometallic ions and organic ligands on the hydrolysis and complexation of thorium ions. However, the strong chelating capacity of organic ligands in these systems often leads to Th^{4+} ions being primarily coordinated by the ligands themselves [41–44]. The chelated Th^{4+} ions are then attached to the central aluminum or iron core *via* bridging oxygen atoms or hydroxyl groups.

Notably, the isolated influence of heterometallic ions on the formation and structures of thorium-containing clusters has mostly been uninvestigated [43]. Al^{3+} ions readily hydrolyze to form various polynuclear species at pH > 3. Moreover, aluminum ores such as bauxite contain significantly higher thorium content compared to thorium's average crustal abundance, with most thorium occurring in grains of stable minerals like zircon and a fraction adsorbed onto alumina minerals [47,48]. Although this adsorption behavior affects thorium's environmental mobility, the underlying molecular-scale mechanisms remain poorly understood [43].

Building on the above research background, we have developed a synthetic strategy involving introducing Th^{4+} ions into an aluminate solution to regulate their hydrolysis and condensation. Al^{3+} ions in this solution already reach hydrolysis equilibrium and exist in the form of polynuclear species [49]. This solution thereby serves a dual role: acting as a pH buffer and supplying aluminate groups that function as ligands, promoting the assembly of Th clusters. Through this approach, we successfully synthesized six electropositive Keggin-type thorium-oxo clusters, $M@Th_{12}@Al_8$, with a substitutable MO_6 center (M = Al, $W_{0.69}Al_{0.31}$, Mo, V, $Cr_{0.14}Al_{0.86}$, and Mn). Given the chemical similarity between aluminum and gallium, we extended this methodology to a mixed aluminate and gallate solution. This modification enabled partial substitution of shell Al atoms by Ga atoms, yielding three electropositive $M@Th_{12}@Ga_mAl_n$ clusters (M = W, Mo, and V; $m+n=8$).

Herein, we report syntheses, structures, optical properties, and self-assembly of the nine $M@Th_{12}@L_8$ ($L_8 = Al_8$ or Ga_mAl_n with $m+n=8$) clusters. This work is of great interest to us for the following reasons:



Scheme 1. Synthetic route of $M@Th_{12}@L_8$ clusters: solutions containing thorium salt and templated ions were mixed with an Al or Al/Ga stock solution; then a mineralizer was added to the solution; crystals of $M@Th_{12}@L_8$ were obtained after a certain period.

(1) This work advances our understanding of thorium hydrolysis and establishes a modular strategy for designing thorium-oxo clusters with tunable architectures and tailored properties.
(2) The obtained nine novel clusters constitute the first electropositive Keggin-type actinide-containing clusters featuring both a substitutable central MO_6 octahedron and tunable shell ligands.
(3) These clusters represent the high nuclear thorium-oxo clusters constructed from three concentric Platonic layers, as opposed to the conventional $M_6(O/OH)_8$ subunits found in most tetravalent metal oxo clusters.
(4) These clusters represent rare multinary heterometallic clusters incorporating main group, transition metal, and actinide elements.
(5) These clusters exhibit distinct optical properties depending on the identity of the central MO_6 octahedron.
(6) Research on thorium-oxo cluster formation remains scarce. Using time-resolved SAXS and ^{27}Al MAS NMR, we observed simultaneous partial decomposition of precursor aluminate clusters and self-assembly of $M@Th_{12}@L_8$ clusters, which stabilize in solution post-formation.

As shown in Scheme 1 and detailed in the Synthetic Procedures section (Supporting information), solutions of thorium nitrate and tris(hydroxymethyl)aminoethane (Tris) were added to an aluminum solution, which was prepared using a reported method [49]. The resulting mixture was heated at 80 °C for 16 h and then cooled to room temperature. Subsequently, disodium 2,6-naphthalenedisulfonate (2,6-NDS-Na_2) was introduced to serve as a crystallization mineralizer. Slow evaporation of the resulting solution at ambient temperature over three days yielded crystals with the formula $[(AlO_6)Th_{12}(OH)_{12}(AlO(OH)_3H_2O)_8(H_2O)_{12}]\cdot(2,6\text{-}NDS)_5\cdot Cl\cdot 37H_2O$ (designated as $Al@Th_{12}@Al_8$). This formula was determined by single crystal X-ray diffraction, elemental analysis, oxidation state characterization, and thermogravimetric analysis (TGA).

Single crystal X-ray diffraction data revealed that $Al@Th_{12}@Al_8$ crystallizes in the triclinic space group $P\bar{1}$ (Table 1 and Table S1 in Supporting information). Its structure features a novel hybrid Al-Th cluster comprising three concentric Platonic-like layers (Figs. 1a-c), with a diameter of 14.838 Å (Fig. S1 in Supporting information). The center is an AlO_6 octahedron (Fig. 1d). The middle layer is an icosahedron (Th_{12}) formed by 12 thorium polyhedra (Fig. 1e), with an average Th···Th distance of 3.8984 Å (Table S2 in Supporting information). The outer layer is a cube (Al_8) constructed from eight AlO_5 polyhedra (Fig. 1f), with an average Al···Al distance of 6.3458 Å (Table S3 in Supporting information). Such a nested Platonic structure in $Al@Th_{12}@Al_8$ is unprecedented in actinide-oxo clusters. The pursuit of metal-oxo clusters with Platonic structure is a goal sought after by synthetic chemists due to the high symmetry and aesthetically pleasing appearance of such structures [50], and our work greatly enriches this family. More interestingly, Th_{12} represents not only the first thorium cluster with icosahedral

Table 1
Crystallographic data and formulas for $M@Th_{12}@L_8$ crystals.

Compounds	Formula	Space group	$a/b/c$ [Å]	$\alpha/\beta/\gamma$ [°]	CCDC
$Al@Th_{12}@Al_8$	$[(AlO_6)Th_{12}(OH)_{12}(AlO(OH)_3H_2O)_8(H_2O)_{12}]\cdot(2,6\text{-}NDS)_5\cdot Cl\cdot 37H_2O$	$P\bar{1}$	15.7913(6) 16.2416(7) 18.5791(8)	108.961(1) 96.252(1) 112.251(1)	2440,934
$W_{0.69}Al_{0.31}@Th_{12}@Al_8$	$[(W_{0.69}Al_{0.31}O_6)Th_{12}(OH)_{12}(AlO(OH)_3H_2O)_8(H_2O)_{12}]\cdot(2,6\text{-}NDS)_6\cdot 1.07Cl\cdot 38H_2O$	$P\bar{1}$	15.6216(5) 18.5440(6) 20.1398(7)	116.2980(10) 100.4570(10) 94.2680(10)	2440,935
$Mo@Th_{12}@Al_8$	$[(MoO_6)Th_{12}(OH)_{12}(AlO(OH)_3H_2O)_8(H_2O)_{12}]\cdot(2,6\text{-}NDS)_6\cdot 2Cl\cdot 43H_2O$	$P\bar{1}$	15.6113(4) 18.5198(5) 20.1694(6)	116.2710(10) 100.4920(10) 94.2700(10)	2440,936
$V@Th_{12}@Al_8$	$[(VO_6)Th_{12}(OH)_{12}(AlO(OH)_3H_2O)_8\ (H_2O)_{12}]\cdot(2,6\text{-}NDS)_6\cdot Cl\cdot 39H_2O$	$P\bar{1}$	15.5993(5) 18.5446(6) 20.2190(6)	115.0740(10) 100.5770(10) 94.4910(10)	2440,937
$Cr_{0.14}Al_{0.86}@Th_{12}@Al_8$	$[(Cr_{0.14}Al_{0.86}O_6)Th_{12}(OH)_{12}(AlO(OH)_3H_2O)_8(H_2O)_{12}]\cdot(2,6\text{-}NDS)_5\cdot Cl\cdot 35H_2O$	$P\bar{1}$	15.7066(7) 16.1913(9) 18.7098(10)	108.865(2) 96.271(2) 112.122(2)	2440,938
$Mn@Th_{12}@Al_8$	$[(MnO_6)Th_{12}(OH)_{12}(AlO(OH)_3H_2O)_8(H_2O)_{12}]\cdot(2,6\text{-}NDS)_5\cdot 2Cl\cdot 35H_2O$	$P\bar{1}$	17.5551(9) 20.7465(11) 23.2198(12)	74.509(2) 85.344(2) 82.050(2)	2440,939
$W@Th_{12}@Ga_{3.69}Al_{4.31}$	$[(WO_6)Th_{12}(OH)_{12}(Ga_{3.69}Al_{4.31}(O(OH)_3H_2O)_8)(H_2O)_{12}]\cdot(2,7\text{-}NDS)_5\cdot 4Cl\cdot 38H_2O$	$P\bar{1}$	15.6236(11) 17.3098(14) 18.8235(14)	67.512(2) 79.724(2) 69.668(2)	2440,940
$Mo@Th_{12}@Ga_{4.43}Al_{3.57}$	$[(MoO_6)Th_{12}(OH)_{12}(Ga_{4.43}Al_{3.57}(O(OH)_3H_2O)_8)(H_2O)_{12}]\cdot(2,7\text{-}NDS)_5\cdot 4Cl\cdot 38H_2O$	$P\bar{1}$	15.6787(7) 17.0746(8) 18.8293(8)	65.714(2) 79.270(2) 70.639(2)	2440,941
$V@Th_{12}@Ga_{4.85}Al_{3.15}$	$[(VO_6)Th_{12}(OH)_{12}(Ga_{4.85}Al_{3.15}(O(OH)_3H_2O)_8)(H_2O)_{12}]\cdot(2,7\text{-}NDS)_6\cdot Cl\cdot 37H_2O$	$P2_1/c$	16.0864(2) 30.0580(4) 20.8001(3)	90 93.7110(10) 90	2440,942

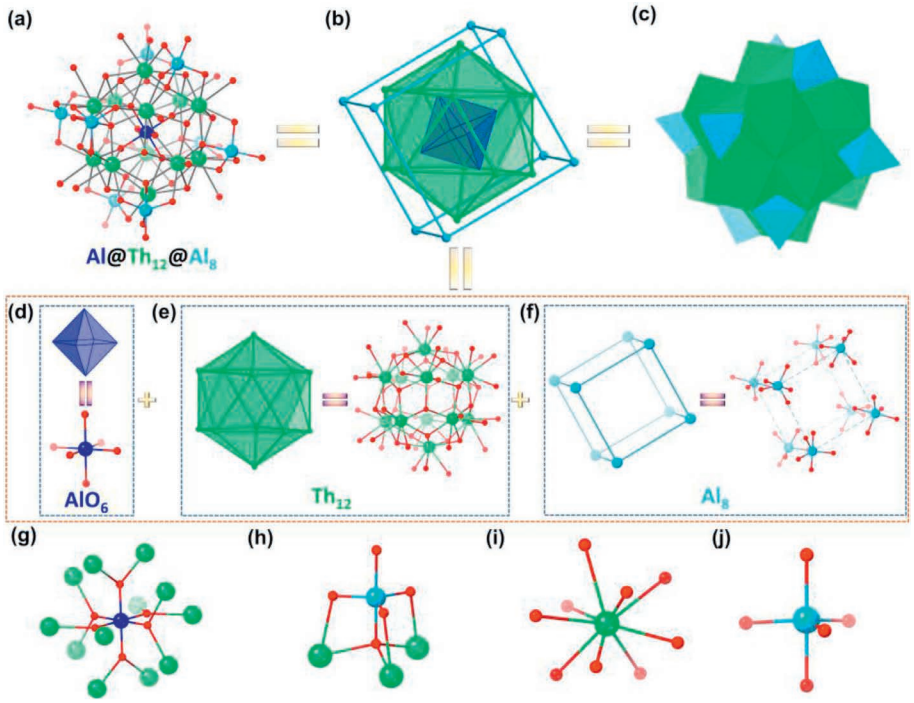


Fig. 1. (a) Ball-stick, (b) graphical, and (c) polyhedral representations of the crystal structure of $Al@Th_{12}@Al_8$, and its three concentric Platonic layers: (d) Central octahedron, (e) thorium icosahedron, and (f) aluminum cubic. (g) Connection of the central AlO_6 group to twelve thorium ions *via* six μ_3-O. (h) Coordination of each AlO_5 group to three thorium ions *via* three μ_2-OH and one μ_4-O. (i) Nine-coordination mode of each Th^{4+} ion. (j) Peripheral AlO_5 group. Color code: Th, green; central Al, blue; peripheral Al, cyan; O, red.

configuration, but also the highest-nuclearity thorium-oxo cluster reported to date. Furthermore, the structure of $Al@Th_{12}$ could be envisioned as four thorium trimers connected to the central AlO_6 octahedron (Fig. S2 in Supporting information). This arrangement of thorium polyhedra is very similar to that in α-Keggin-type clusters like Al_{13} (Fig. S2) [51,52]. Therefore, $Al@Th_{12}@Al_8$ represents the first α-Keggin-type actinide-oxo cluster, stabilized by AlO_5 groups.

A closer examination of the structure of $Al@Th_{12}@Al_8$ and bond valence sum (BVS) analysis of the coordinated O atoms reveals that the Al^{3+} ion in the central symmetric octahedron is coordinated by six μ_3-O atoms, with Al-O bond lengths ranging from 1.8645 Å to 1.8707 Å (Tables S4 and S5, Fig. S23 in Supporting information). In addition to this Al^{3+} ion, each of the six μ_3-O atoms is also coordinated with two Th^{4+} ions, connecting the central octahedron and middle icosahedron (Fig. 1g). The remaining coordination sites

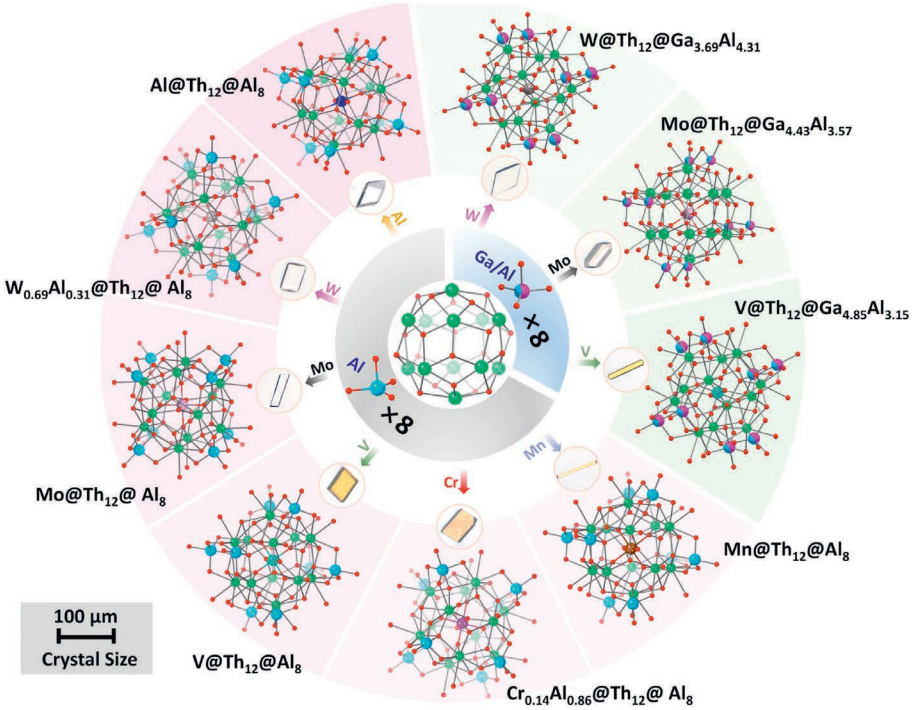


Fig. 2. Crystals and structures of six $M@Th_{12}@Al_8$ (M = Al, $W_{0.69}Al_{0.31}$, Mo, V, $Cr_{0.14}Al_{0.86}$, or Mn) clusters and three $M@Th_{12}@Ga_mAl_n$ (M = W, Mo, or V) clusters with a variable central MO_6 octahedron. Color code: Th, green; central Al, blue; peripheral Al, cyan; W, grey; Mo, grey pink; V, light blue; Cr, purple; Mn, brown; Ga, pink; O, red.

of each Th^{4+} ions are occupied by two μ_2-OH groups and two μ_4-O atoms from two AlO_5 groups in the cube, three μ_3-OH groups, and one H_2O molecule (Fig. 1i), with an average Th-O bond length of 2.4726 Å (Table S2). Compared to the symmetric octahedral coordination geometry of central AlO_6, the AlO_5 is asymmetric. Its five O atoms are assigned as one μ_4-O atom, three μ_2-OH group, and one H_2O molecule (Fig. 1j), with average bond lengths of Al-(μ_4-O) = 1.8919 Å, Al-(μ_2-OH) = 1.7940 Å, Al-(OH_2) = 1.9134 Å (Table S3). Each AlO_5 group is connected to three Th^{4+} ions through one μ_4-O atom and three μ_2-OH groups (Fig. 1h), passivating the surface of Th_{12}.

A significant characteristic of classical transition metal (*e.g.*, W and Mo) Keggin-type POMs is that their central polyhedron serves as a template for their formation and is substitutable [53]. In addition to Al_{13} [51], limited research has been conducted on the role and properties of central polyhedra in recently reported Keggin-type clusters (*e.g.*, Fe_{13} [8], Mn_{13} [9], Zr_{13} [10], Hf_{13} [11], and Eu_{13} [12]). In this study, to elucidate the role of the central AlO_6 octahedron in cluster $Al@Th_{12}@Al_8$, we systematically introduced nearly all accessible transition metal salts into its reaction solution (Synthetic Procedures section in Supporting information). As shown in Fig. 2, we ultimately obtained crystals of five new clusters, designated as $M@Th_{12}@Al_8$ (M = $W_{0.69}Al_{0.31}$, Mo, V, $Cr_{0.14}Al_{0.86}$, and Mn). These crystals have similar formulas (Table 1 and Table S1). Notably, they exhibit topological structures similar to $Al@Th_{12}@Al_8$, primarily differing in their central MO_6 octahedra (Fig. 2 and Figs. S3-S7 in Supporting information). This demonstrates that the central MO_6 octahedra in $M@Th_{12}@Al_8$ are substitutable.

Since the ligands of some tetravalent metal-oxo clusters like Th_6 are substitutable, we also conducted syntheses using mixed solutions containing aluminate-gallate or aluminate-germanate. As shown in Table 1 and Table S1, only the aluminate-gallate solution proved effective, yielding crystals of three new clusters: $M@Th_{12}@Ga_mAl_n$ (M = W, Mo, and V; $m+n=8$). These clusters exhibit structures similar to $M@Th_{12}@Al_8$, with the key difference being the substitution of some AlO_5 groups by GaO_5 groups (Fig. 2 and Figs. S8-S10 in Supporting information). This suggests that the AlO_5 (or GaO_5) groups in the series of $M@Th_{12}@L_8$ (M = Al, $W_{0.69}Al_{0.31}$, Mo, V, $Cr_{0.14}Al_{0.86}$, and Mn; $L_8 = Al_8$ or Ga_mAl_n with $m+n=8$) clusters act as tunable ligands.

To our knowledge, $M@Th_{12}@L_8$ represents the first series of Keggin-type actinide-containing clusters with both a substitutable central polyhedron and tunable shell ligands. Among the series of $M@Th_{12}@L_8$ clusters, $Mo@Th_{12}@Al_8$ exhibits the fastest crystallization rate (within hours) and highest yields (up to 70.2 %). In contrast, $Mn@Th_{12}@Al_8$ formed at the highest solution pH of 5.19, where thorium hydroxides precipitate [54]. These results indicate that the identity of the central metal ions affects the formation and yield of $M@Th_{12}@L_8$ clusters.

It is noteworthy that the nine clusters exhibit a co-occupation phenomenon. Specifically, the central M ion in $W_{0.69}Al_{0.31}@Th_{12}@Al_8$ is co-occupied by W and Al ions, and that in $Cr_{0.14}Al_{0.86}@Th_{12}@Al_8$ is co-occupied by Cr and Al ions. Additionally, several shell L ions in $M@Th_{12}@Ga_mAl_n$ are co-occupied by Al and Ga ions. Similar co-occupation phenomena are also common in mineral structures [55].

More remarkably, we found that the Al-O, W-O, Mo-O, V-O, Cr-O, and Mo-O bond lengths for the central octahedra in $M@Th_{12}@L_8$ clusters consistently measure ~1.87 Å, despite significant variations reported for these bonds in other structures (Table S4 in Supporting information). For example, V-O bonds in literature span 1.67–2.49 Å [56]. Furthermore, the diameters of $M@Th_{12}@Al_8$ remain constant (~14.85 Å) regardless of the central MO_6 octahedron type (Figs. S1 and S8-S10 in Supporting information). Similarly, $M@Th_{12}@Ga_mAl_n$ clusters maintain slightly larger fixed diameters (~15.00 Å), due to the larger radius of Ga^{3+} compared to Al^{3+} (Figs. S8-S10 in Supporting information). These results demonstrate the structural rigidity of $M@Th_{12}@L_8$ clusters, which imposes strict geometric constraints on central metal ion coordination. By contrast, in classic Keggin-type clusters XW_{12}, the X-O bond lengths within their central XO_4 tetrahedra vary significantly depending on the identity of the heteroatom X [57].

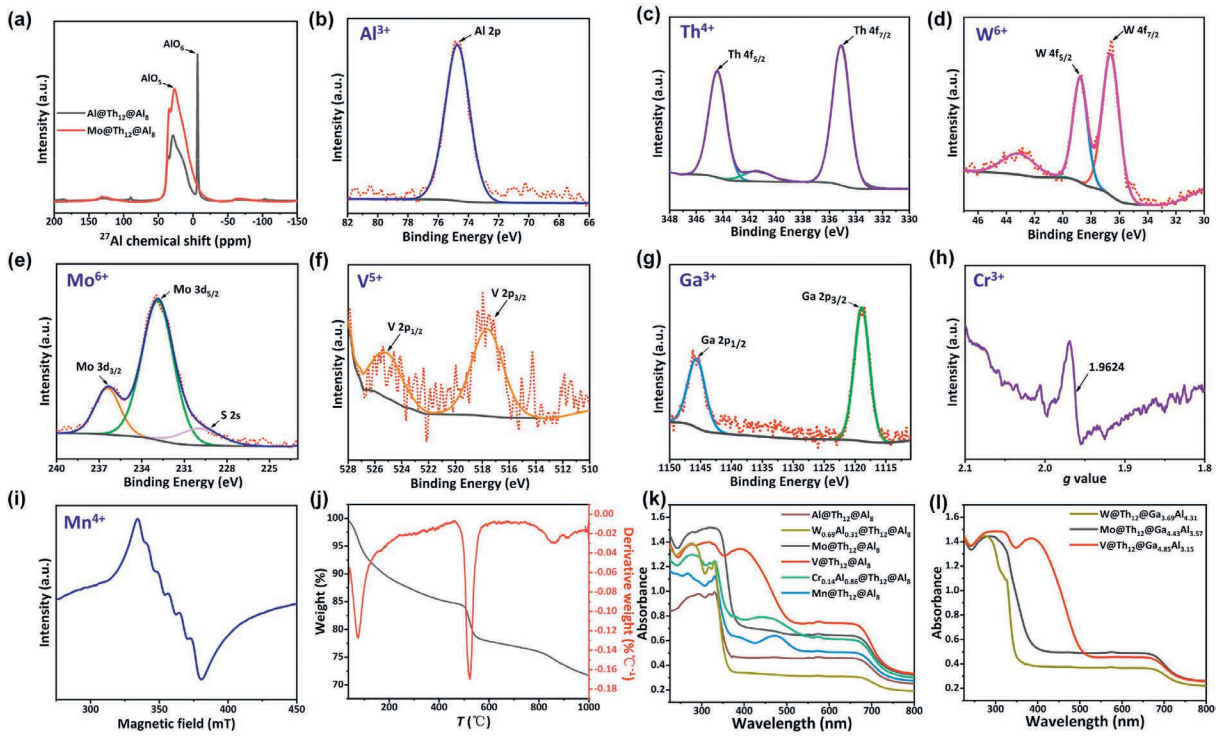


Fig. 3. (a) Solid state ^{27}Al MAS NMR spectra of Al@Th_{12}@Al_8 and Mo@Th_{12}@Al_8. (b-g) Representative XPS high-resolution spectra of Al, Th, W, Mo, V, and Ga in M@Th_{12}@L_8. (h) EPR spectra of Cr in $Cr^{3+}_{0.14}Al^{3+}_{0.86}$@$Th_{12}$@$Al_8$ and (i) Mn in Mn@Th_{12}@Al_8. (j) TGA curves of Al@Th_{12}@Al_8. UV–vis spectra of (k) M@Th_{12}@Al_8 and (l) M@Th_{12}@Ga_mAl_n.

Structural analysis of the nine M@Th_{12}@L_8 clusters reveals that they adopt a general formula of $[(MO_6)Th_{12}(OH)_{12}(LO(OH)_3H_2O)_8(H_2O)_{12}]^{(8+x)+}$, where x represents the charge of the central metal ion. According to BVS analysis, the central metal ions were identified as Al^{3+}, Cr^{3+}, Mn^{4+}, V^{5+}, Mo^{6+}, and W^{6+}, resulting in the cluster charges ranging from +11 to +14 (Tables S25 and S26 in Supporting information). This is in stark contrast to most POMs, which are typically negatively charged [2]. The unusual positive charges of these clusters are balanced by Cl^- and 2,6-NDS (or 2,7-NDS) anions dispersed among them (Figs. S11-S20 in Supporting information). The periodic arrangement of 2,6-NDS (or 2,7-NDS) anions, along with the 3.5–3.8 Å spacing between their naphthalene rings, indicates the presence of $\pi-\pi$ stacking [58].

To complement the single crystal X-ray diffraction data, multiple techniques were employed to further characterize the structure, composition, and properties of M@Th_{12}@L_8 crystals. The powder X-ray diffraction (PXRD) patterns were used to investigate the purity and crystallinity of these crystals (Figs. S21-S29 in Supporting information). Solid-state ^{27}Al MAS NMR spectroscopy was used to confirm the coordination environments of Al^{3+}. As shown in Fig. 3a, the spectrum of Al@Th_{12}@Al_8 exhibits a broad peak at ~26 ppm and a sharp peak at −6 ppm. This broad peak is assigned to shell AlO_5 groups [59,60], with its line broadening originating from the asymmetric coordination geometry of the shell Al ions. By contrast, the sharp peak is attributed to the central AlO_6 groups [59]. The narrow linewidth and high intensity of this resonance reflect the highly symmetric octahedral coordination environment of the central Al^{3+} ion, a rare feature among aluminum-based clusters. AlO_5 groups in Al clusters typically adopt asymmetric configurations due to mixed coordination with O atoms, OH groups, and H_2O molecules, resulting in broad NMR peaks [51]. The unusually sharp resonance observed here for the AlO_6 group in Al@Th_{12}@Al_8 is thus distinctive and can serve as a diagnostic marker for this cluster. Notably, the spectrum of Mo@Th_{12}@Al_8 exhibits only the AlO_5 resonance, consistent with its lack of central AlO_6.

Table 2
The summary of ICP-MS results for M@Th_{12}@L_8 crystals.

Sample	Elements	Experimental ratios	Calculated ratios
Al@Th_{12}@Al_8	Al:Th	10.80:12.00	9:12
$W_{0.69}Al_{0.31}$@Th_{12}@Al_8	W:Al:Th	0.41:7.07:12.00	0.69:8.31:12
Mo@Th_{12}@Al_8	Mo:Al:Th	1.07:8.63:12.00	1:8:12
V@Th_{12}@Al_8	V:Al:Th	0.96:7.89:12.00	1:8:12
$Cr_{0.14}Al_{0.86}$@Th_{12}@Al_8	Cr:Al:Th	0.34:7.72:12.00	0.14:8.86:12
Mn@Th_{12}@Al_8	Mn:Al:Th	0.88:7.17:12.00	1:8:12
W@Th_{12}@$Ga_{3.69}Al_{4.31}$	W:Al:Ga:Th	1.00:4.88:3.41:12.00	1:4.31:3.69:12
Mo@Th_{12}@$Ga_{4.43}Al_{3.57}$	Mo:Al:Ga:Th	0.99:4.65:3.56:12.00	1:3.57:4.43:12
V@Th_{12}@$Ga_{4.85}Al_{3.15}$	V:Al:Ga:Th	0.57:3.66:3.63:12.00	1:3.15:4.85:12

Scanning electron microscopy-energy dispersive X-ray spectroscopy (SEM-EDS) data qualitatively confirmed the existence of C, N, O, S, Al, Ga, Th, and central transition metal elements (*e.g.*, W, Mo, V, Cr, and Mn) in these crystals (Figs. S30-S38 in Supporting information). For quantitative characterization of the metal content, inductively coupled plasma-mass spectrometry (ICP-MS) was performed. As summarized in Table 2 and Tables S27 and S28 (Supporting information), the measured molar ratios of metal elements in M@Th_{12}@L_8 were consistent with the calculated values, thereby verifying the accuracy of the chemical formulas presented in Table 1.

In addition to BVS analysis (Tables S25 and S26 in Supporting information), X-ray photoemission spectroscopy (XPS) was employed to confirm the oxidation states of metal ions in M@Th_{12}@L_8 crystals. The obtained full-scan and high-resolution XPS spectra (Figs. 3b-g and Figs. S39-S47 in Supporting information) demonstrate the presence of Al^{3+}, Ga^{3+}, Th^{4+}, W^{6+}, Mo^{6+}, V^{5+}, Mn^{4+}, and S^{6+}, with detailed peak assignments summarized in Table 3. Due to the low Cr content in $Cr_{0.14}Al_{0.86}$@Th_{12}@Al_8, collecting a reliable high-resolution XPS spectrum was challenging. Therefore, electron paramagnetic resonance (EPR) was used to further characterize this compound. The obtained EPR spectrum exhibits a broad signal centered at $g = 1.9624$ (Fig. 3h). This signal is consistent with

Table 3
XPS peak positions and assignments for Al [63], Th [29], Ga [64], W [65], Mo [66], V [67], Cr [68], and Mn [62] ions in $M@Th_{12}@L_8$ crystals.

Sample	XPS peak positions (eV) and assignments						
$Al@Th_{12}@Al_8$	74.77 (Al 2p)	344.47 (Th $4f_{5/2}$)	335.17 (Th $4f_{7/2}$)				
$W_{0.69}Al_{0.31}@Th_{12}@Al_8$	74.97 (Al 2p)	344.67 (Th $4f_{5/2}$)	335.37 (Th $4f_{7/2}$)	38.77 (W $4f_{5/2}$)	36.57 (W $4f_{7/2}$)		
$Mo@Th_{12}@Al_8$	74.77 (Al 2p)	344.37 (Th $4f_{5/2}$)	335.17 (Th $4f_{7/2}$)	236.37 (Mo $3d_{3/2}$)	232.87 (Mo $3d_{5/2}$)		
$V@Th_{12}@Al_8$	74.77 (Al 2p)	344.47 (Th $4f_{5/2}$)	335.07 (Th $4f_{7/2}$)	525.37 (V $2p_{1/2}$)	517.67 (V $2p_{3/2}$)		
$Cr_{0.14}Al_{0.86}@Th_{12}@Al_8$	74.57 (Al 2p)	344.27 (Th $4f_{5/2}$)	334.97 (Th $4f_{7/2}$)	581.67 (Cr $2p_{1/2}$)	575.87 (Cr $2p_{3/2}$)		
$Mn@Th_{12}@Al_8$	74.57 (Al 2p)	344.27 (Th $4f_{5/2}$)	334.97 (Th $4f_{7/2}$)	653.87 (Mn $2p_{1/2}$)	624.77 (Mn $2p_{3/2}$)		
$W@Th_{12}@Ga_{3.69}Al_{4.31}$	74.50 (Al 2p)	344.50 (Th $4f_{5/2}$)	335.20 (Th $4f_{7/2}$)	38.20 (W $4f_{5/2}$)	36.10 (W $4f_{7/2}$)	1145.2 (Ga $2p_{1/2}$)	1118.4 (Ga $2p_{3/2}$)
$Mo@Th_{12}@Ga_{4.43}Al_{3.57}$	75.20 (Al 2p)	345.10 (Th $4f_{5/2}$)	335.70 (Th $4f_{7/2}$)	236.17 (Mo $3d_{3/2}$)	232.67 (Mo $3d_{5/2}$)	1145.9 (Ga $2p_{1/2}$)	1119.0 (Ga $2p_{3/2}$)
$V@Th_{12}@Ga_{4.85}Al_{3.15}$	74.50 (Al 2p)	344.30 (Th $4f_{5/2}$)	335.00 (Th $4f_{7/2}$)	525.87 (V $2p_{1/2}$)	518.47 (V $2p_{3/2}$)	1145.3 (Ga $2p_{1/2}$)	1118.50 (Ga $2p_{3/2}$)

the *g* value of standard $CrCl_3$ [61], confirming the presence of Cr^{3+}. Similarly, the six-line hyperfine splitting in the EPR spectrum of $Mn@Th_{12}@Al_8$ further verifies the presence of Mn^{4+} (Fig. 3i) [62]. All the above experimental data align well with the BVS analysis results, providing consistent evidence for the assigned oxidation states.

The Fourier transform infrared (FT-IR) spectra of $M@Th_{12}@L_8$ crystals exhibit similar vibrational peaks in the 4000–400 cm^{-1} range, confirming the presence of solvent water molecules, coordinated hydroxyl groups, and 2,6-NDS/2,7-NDS (Figs. S48 and S49 in Supporting information). Specifically, the broad envelope at 3385 cm^{-1} corresponds to vibrations from solvent water molecules [69]. The peak at 1635 cm^{-1} arises from bending modes of coordinated hydroxyl groups [69]. Peaks in the 1200–1000 cm^{-1} range are assigned to sulfonate groups of 2,6-NDS or 2,7-NDS [69]. Peaks in the 900–750 cm^{-1} range are attributed to the C–H in-plane or out-of-plane bending, ring deformation, and ring breathing of naphthalene in 2,6-NDS or 2,7-NDS [70]. The peak at 700 cm^{-1} is assigned to the stretching vibrations of Al(Ga)-O bonds; the peaks at 658 and 618 cm^{-1} are attributed to the stretching vibrations of Al-OH bonds; the weak peak around 511 cm^{-1} corresponds to the stretching vibrations of Al-OH_2 bonds [71].

Thermogravimetric analysis (TGA) was employed to quantify the solvent water content and evaluate the thermal stability of $M@Th_{12}@L_8$ crystals. As shown in Fig. 3j and Figs. S50-S57 (Supporting information), these crystals exhibit similar TGA plots. Using $Al@Th_{12}@Al_8$ as an example, a weight loss of 10.67 % between 33 and 200 °C corresponds to the removal of 37 solvent water molecules per formula unit [35]. Further weight loss in the range of 200–400 °C is attributed to the release of coordinated water molecules and hydroxyl groups [72]. The sharp weight loss at 520 °C is related to the decomposition of 2,6-NDS, particularly the combustion of naphthalene rings [72]. The calculated number of solvent water molecules for each crystal is summarized in Table 1. Additionally, the residues remaining after TGA were analyzed using PXRD (Fig. S58 in Supporting information). The obtained patterns confirm the presence of crystalline ThO_2, while previous studies suggest that the residues may also contain amorphous Al_2O_3 [72].

The solid-state ultraviolet-visible (UV–vis) spectra of the nine $M@Th_{12}@L_8$ clusters reveal that clusters with AlO_6, MoO_6, or WO_6 centers exhibit strong absorption exclusively in the UV region, attributed to oxygen-to-metal charge transfer [73]. In contrast, those with VO_6, CrO_6, or MnO_6 centers show additional absorption in the visible region (Figs. 3k and l). For $V@Th_{12}@L_8$ and $Cr_{0.14}Al_{0.86}@Th_{12}@Al_8$, the absorption peaks at 390 and 450 nm are attributed to the $d \rightarrow d$ electronic transitions of V^{5+} and Cr^{3+} [74],

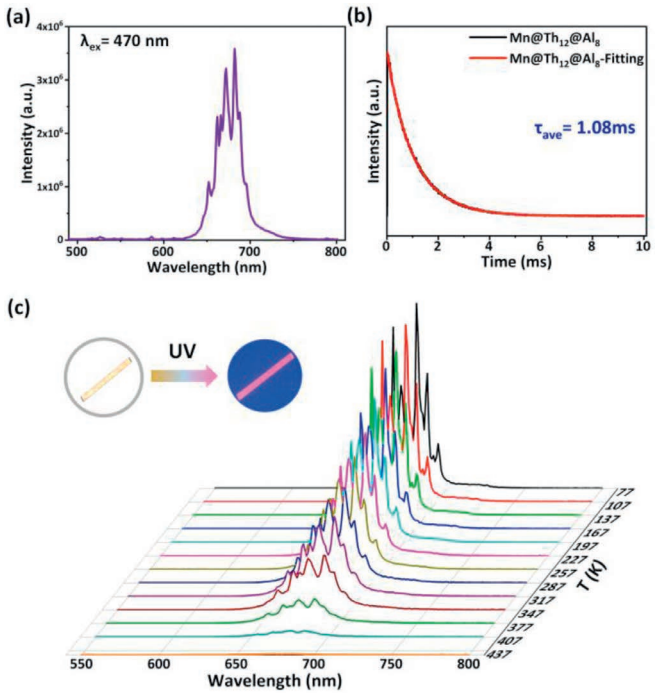


Fig. 4. (a) Photoluminescence emission spectrum, (b) fluorescence lifetime, and (c) temperature-dependent photoluminescence emission spectra of $Mn@Th_{12}@Al_8$.

while the absorption at 470 nm for $Mn@Th_{12}@Al_8$ is assigned to the charge transfer transition of $^4A_{2g} \rightarrow {}^4T_{1g}$ and $^4A_{2g} \rightarrow {}^4T_{2g}$ of Mn^{4+} ions [75]. This difference highlights the significant influence of the central metal ions on the optical properties of these clusters. Furthermore, the optical band gaps of these clusters, calculated using the Kubelka–Munk function [76], range from 2.37 eV to 3.60 eV (Figs. S59-S67 in Supporting information). These values suggest their semiconducting properties [77].

Furthermore, the photoluminescence properties of $Mn@Th_{12}@Al_8$ crystals were investigated using steady-state transient fluorescence spectroscopy, as they exhibit prominent pink fluorescence under illumination. As shown in Fig. 4a and Fig. S68 (Supporting information), these crystals exhibit multiple intense peaks in the region of 625–750 nm upon excitation at 470 nm. This distinct photoluminescence behavior originates from the $^2E_g \rightarrow {}^4A_{2g}$ transition of Mn^{4+} center [78], with a fluorescence lifetime of 1.08 milliseconds and the quantum yield of 39.77 %

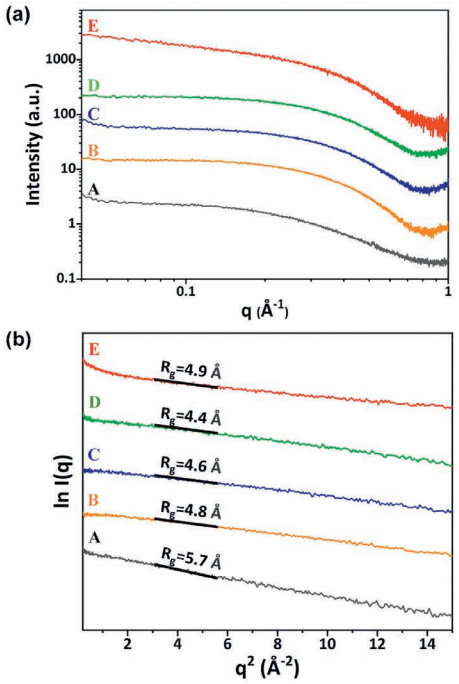


Fig. 5. (a) SAXS and (b) Guinier plots for solutions related to synthesis and crystals of $M@Th_{12}@Al_8$: (A) Aluminate stock solution; (B) mixture of aluminate stock solution, thorium nitrate solution, and tris(hydroxymethyl)aminoethane after heating at 80 °C); (C) aforementioned mixed solution with the addition of 2,6-NDS-Na_2; (D) centrifuged solution after the formation of $Al@Th_{12}@Al_8$ crystals; (E) solution obtained by dissolving $Al@Th_{12}@Al_8$ crystals into tetrabutylammonium bromide solution.

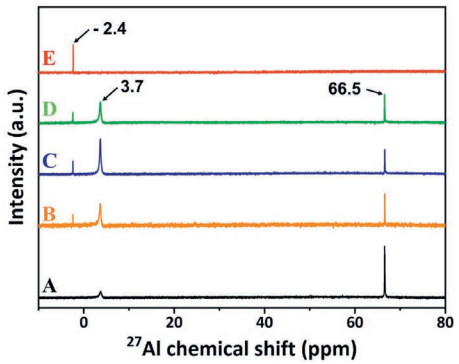


Fig. 6. ^{27}Al solution NMR plots for solutions related to synthesis and crystals of $Al@Th_{12}@Al_8$. The sample labels are the same as in Fig. 5.

(Fig. 4b and Fig. S69 in Supporting information). Furthermore, temperature-dependent luminescence spectra of this cluster show a gradual decrease in emission intensity as the temperature increases from 77 K to 437 K (Fig. 4c and Fig. S70 in Supporting information). Notably, when measured $Mn@Th_{12}@Al_8$ crystals using PXRD after thermal cycling, the obtained data demonstrate their good thermal stability (Fig. S71 in Supporting information).

The above results suggest that the optical properties of $M@Th_{12}@L_8$ clusters can be effectively modulated by varying the central metal ion. On the other hand, these clusters with distinct optical properties show promising potential in many applications, such as the preparation of stable Mn^{4+}-doped phosphors, as the Th_{12} layer provides excellent protection for the Mn^{4+} luminescence centers [79].

The stability of the representative $M@Th_{12}@Al_8$ cluster was investigated using time-resolved SAXS (Fig. 5) and ^{27}Al NMR (Fig. 6). Guinier analysis of the SAXS data provided the radius of gyration (R_g) for each sample [80]. For the solution obtained by dissolving the $Al@Th_{12}@Al_8$ crystals, the R_g value is 4.9 Å. This value agrees well with the theoretical R_g value (4.6 Å) derived from the fitting of the crystallographic data, confirming that the $Al@Th_{12}@Al_8$ cluster remains intact in solution [81]. The NMR spectrum of this solution exhibits a narrow peak at −2.4 ppm, which is attributed to the central symmetric AlO_6 octahedron, further demonstrating the stability of $Al@Th_{12}@Al_8$ in solution.

The self-assembly process of $Al@Th_{12}@Al_8$ clusters in the reaction solution was also investigated using SAXS and NMR (Figs. 5 and 6). For the aluminate solution, the R_g is approximately 5.7 Å, consistent with the presence of nano-sized aluminate clusters in solution [49]. The corresponding NMR spectrum exhibited peaks at 3.7 and 66.5 ppm, which are attributed to asymmetric AlO_6 and symmetric AlO_4 groups in Al clusters, respectively [49]. After adding thorium nitrate solution and Tris to the aluminate solution and heating the mixture, the SAXS profile changes significantly, and the R_g decreases to 4.8 Å, which matches the theoretical value (4.6 Å) derived from the fitting of the crystallographic data of $Al@Th_{12}@Al_8$. Concurrently, a new NMR peak at −2.4 ppm appears, characteristic of the central AlO_6 in $Al@Th_{12}@Al_8$. Meanwhile, the relative intensity of the peak at 66.5 ppm decreases. These results confirm the formation of $Al@Th_{12}@Al_8$ clusters and the partial decomposition of the original aluminate clusters in solution. Subsequent addition of the mineralizer (2,6-NDS) caused no further changes in SAXS or NMR, demonstrating the clusters' stability in solution. Similarly, after crystallization, the SAXS and NMR profiles remained unchanged, further supporting the persistence of $Al@Th_{12}@Al_8$ clusters in solution. According to the SAXS and NMR data, a schematic was prepared to illustrate the assembly process of $Al@Th_{12}@Al_8$ clusters (Fig. S72 in Supporting information).

A striking structural feature of the nine $M@Th_{12}@L_8$ clusters is their tri-layered architecture, in which the central MO_6 octahedron and the middle Th_{12} icosahedron adopt a Keggin-type arrangement. The outer cubic layer consists of eight non-interconnected LO_5 polyhedra that act as inorganic ligands. Although both the central MO_6 and outer LO_5 polyhedra are chemically variable, the M–O bond lengths remain invariant across different M ions. This invariance stems from the clusters' inherent structural rigidity, which imposes strict constraints on the coordination geometry of the central M ion. In contrast, Keggin-type XW_{12}, XMo_{12}, and XAl_{12} clusters feature a variable central XO_4 tetrahedron, where X–O bond lengths depend on the identity of X [51,57]. Other metal-based Keggin clusters, primarily including Fe_{13} [8], Mn_{13} [9], Zr_{13} [10], Hf_{13} [11], and Eu_{13} [12], are stabilized by organic ligands, but the substitutability of their central polyhedra has not been explored (Fig. S73 in Supporting information).

From a compositional perspective, the nine $M@Th_{12}@L_8$ clusters represent rare multinary heterometallic clusters incorporating main group, transition metal, and actinide elements. To our knowledge, only a limited number of thorium-containing heterometallic clusters have been reported. Apart from a few clusters stabilized by lacunary POMs of W and Mo to stabilize thorium ions [40], the known heterometallic clusters primarily include $Th_2Al_6(edta)_2$ [41], $Th_2Al_6(hedta)_2$ [42], $Th_2Al_8(hdpta)$ [42], $Th_2Al_8(heidi)$ [43], $Th_4Al_{10}(edta)$ [41], $ThFe_2(dhpta)$ [43], $Th_2Fe_{10}(PhPO_3)$ [44], $Th_9Ag_6(PyCOO)$ [46], and $Th_9Ag_{12}(PyCOO)$ [46] (Fig. S74 in Supporting information). Among these binary clusters, the Th-Al and Th-Fe clusters form within a pH range of 2.35–5.95 and exhibit structures with a planar Al or Fe core, constructed *via* bridging O atoms and OH groups [41–44]. Th^{4+} ions are primarily chelated by organic ligands and then individually attached to the core. These structural features suggest that the hydrolysis and condensation of Al^{3+} or Fe^{3+} ions drive cluster formation, while chelated Th^{4+} ions function as ligands.

Although the M@Th_{12}@L_8 clusters form in a similar pH range of 3.02–5.19, only their middle Th_{12} layer assembles *via* bridging O atoms and OH groups. This structural distinction implies that the hydrolysis and condensation of Th^{4+} ions direct the assembly of the M@Th_{12}@L_8 clusters, with AlO_5 groups passivating the Th_{12} layer. This conclusion aligns with our SAXS and NMR data, which reveal the simultaneous decomposition of precursor Al clusters and self-assembly of M@Th_{12}@L_8 clusters. The stark structural contrast between reported Th-Al/Fe clusters and our M@Th_{12}@L_8 clusters indicates divergent hydrolysis behaviors and roles of Th^{4+} and Al^{3+} ions in the formation of heterometallic clusters, depending on the presence or absence of organic ligands. Notably, the two Th-Ag clusters contain Th cores with Ag^+ ions attached peripherally. This structural motif is attributed to the identity of Ag^+ ions as soft Lewis acids and their weaker hydrolysis ability [46].

Since M@Th_{12}@L_8 clusters are primarily formed through the hydrolysis and condensation reactions of thorium ions, they can be regarded as thorium-oxo clusters stabilized by AlO_5 ligands. In contrast, most other tetravalent metal-oxo clusters typically exhibit fluorite-like topological structures [23,24], and/or architectures built from octahedral $M_6(O/OH)_8$ subunits (Fig. S75 in Supporting information) [21,33,35]. The distinct tri-layered architecture of M@Th_{12}@L_8 clusters arises from the synergistic effects of the central heterometal (M) and the aluminate ligands. These components collectively modulate the hydrolysis and condensation pathways of Th^{4+} ions, enabling this unprecedented structural motif.

In this study, we report the synthesis of M@Th_{12}@L_8, the first series of electropositive α-Keggin-type thorium-oxo clusters featuring unprecedented triple-layered Platonic architectures: a central MO_6 octahedron, a Th_{12} icosahedron, and an outer LO_5 cube. These clusters represent rare high-nuclearity thorium species and heterometallic systems integrating main-group, transition-metal, and actinide elements. Their structural rigidity ensures constant M–O bond lengths despite variability in central MO_6 octahedra, while the central M ion governs the solution pH during cluster formation, crystallization kinetics, crystal yield, and tunable photoluminescence. Time-resolved SAXS and ^{27}Al MAS NMR reveal the synchronized partial decomposition of precursor Al clusters and concurrent self-assembly of M@Th_{12}@L_8 clusters. This work establishes a platform for designing novel thorium clusters *via* heterometallic ion-regulated hydrolysis, with central/shell substitution enabling tailored properties.

CRediT authorship contribution statement

Chunhui Wang: Writing – original draft, Methodology, Investigation, Formal analysis, Data curation. **Zhe Han:** Data curation. **Yuan Gao:** Data curation. **Chaoyue Fan:** Data curation. **Puyong He:** Data curation. **Bojun Li:** Data curation. **Dong Ma:** Data curation. **Yang Zhang:** Investigation. **Lei Zhang:** Conceptualization. **Jie Qiu:** Writing – review & editing, Visualization, Project administration, Methodology, Funding acquisition, Formal analysis, Data curation, Conceptualization.

Declaration of competing interest

All of the authors reviewed and contributed to this paper. And the authors declare no competing financial interest.

Acknowledgments

This study was funded by the National Natural Science Foundation of China (Nos. 22276147, 22476158, 22076152, 21806127). The authors sincerely acknowledge the Instrumental Analysis Center of Xi'an Jiaotong University for fluorescence tests, the State Key Laboratory of Multiphase Flow in Power Engineering for single-crystal tests using a Bruker D8 Quest diffractometer, and Soochow University for spectroscopy tests.

Supplementary materials

CCDC (2440,934–2440,942) contains the supplementary crystallographic data for this paper. These data can be obtained free of charge via https://www.ccdc.cam.ac.uk/ structures/. Supplementary material associated with this article can be found, in the online version, at doi:10.1016/j.cclet.2025.111563.

References

[1] J.J. Berzelius, Ann. Phys. 82 (1826) 369–392.
[2] D.L. Long, R. Tsunashima, L. Cronin, Angew. Chem. Int. Ed. 49 (2010) 1736–1758.
[3] M. Pascual-Borras, E. Arca, H. Yoshikawa, et al., J. Am. Chem. Soc. 146 (2024) 26485–26496.
[4] K. Uemura, M. Oshika, H. Hasegawa, A. Takamori, M. Sato, Angew. Chem. Int. Ed. 63 (2024) e202407743.
[5] M. Wang, J.Y. Pang, J.P. Wang, J.Y. Niu, Coord. Chem. Rev. 508 (2024) 215730.
[6] A. Muller, F. Peters, M.T. Pope, D. Gatteschi, Chem. Rev. 98 (1998) 239–272.
[7] G. Johansson, G. Lundgren, L.G. Sillen, R. Soderquist, Acta Chem. Scand. 14 (1960) 769–771.
[8] O. Sadeghi, L.N. Zakharov, M. Nyman, Science 347 (2015) 1359–1362.
[9] C. Lampropoulos, C. Koo, S.O. Hill, K. Abboud, G. Christou, Inorg. Chem. 47 (2008) 11180–11190.
[10] B. Morosin, Acta Crystallogr. Sect. B: Struct. Sci. 33 (1977) 303–305.
[11] X.M. Kang, H.S. Hu, Z.L. Wu, et al., Angew. Chem. Int. Ed. 58 (2019) 16610–16616.
[12] K. Sheng, W.D. Si, R. Wang, et al., Chem. Mater. 34 (2022) 4186–4194.
[13] J. Qiu, P.C. Burns, Chem. Rev. 113 (2013) 1097–1120.
[14] U.E. Humphrey, M.U. Khandaker, Renew. Sustain. Energy Rev. 97 (2018) 259–275.
[15] M. Lung, O. Gremm, Nucl. Eng. Des. 180 (1998) 133–146.
[16] A.E. Gorden, J. Xu, K.N. Raymond, P. Durbin, Chem. Rev. 103 (2003) 4207–4282.
[17] G. Creff, S. Safi, J. Roques, et al., Inorg. Chem. 55 (2016) 29–36.
[18] K.E. Knope, L. Soderholm, Chem. Rev. 113 (2013) 944–994.
[19] S. Takao, K. Takao, W. Kraus, et al., Eur. J. Inorg. Chem. 2009 (2009) 4771–4775.
[20] C. Walther, M.A. Denecke, Chem. Rev. 113 (2013) 995–1015.
[21] S. Øien-Ødegaard, C. Bazioti, E.A. Redekop, et al., Angew. Chem. Int. Ed. 59 (2020) 21397–21402.
[22] B. Russell-Webster, J. Lopez-Nieto, K.A. Abboud, G. Christou, Angew. Chem. Int. Ed. 60 (2021) 12591–12596.
[23] L. Soderholm, P.M. Almond, S. Skanthakumar, R.E. Wilson, P.C. Burns, Angew. Chem. Int. Ed. 47 (2008) 298–302.
[24] N.P. Martin, C. Volkringer, P. Roussel, et al., Chem. Commun. 54 (2018) 10060–10063.
[25] K.E. Knope, R.E. Wilson, M. Vasiliu, D.A. Dixon, L. Soderholm, Inorg. Chem. 50 (2011) 9696–9704.
[26] Y.J. Hu, K.E. Knope, S. Skanthakumar, L. Soderholm, Eur. J. Inorg. Chem. 2013 (2013) 4159–4163.
[27] N.A. Vanagas, J.N. Wacker, C.L. Rom, et al., Inorg. Chem. 57 (2018) 7259–7269.
[28] H. Lu, M. Xu, Z. Zheng, et al., Inorg. Chem. 60 (2021) 18629–18633.
[29] Q. Niu, Q. Huang, T.Y. Yu, et al., J. Am. Chem. Soc. 144 (2022) 18586–18594.
[30] K.E. Knope, M. Vasiliu, D.A. Dixon, L. Soderholm, Inorg. Chem. 51 (2012) 4239–4249.
[31] X.Y. Qian, T.H. Zhou, J.G. Mao, Dalton Trans. 44 (2015) 13573–13580.
[32] P. Woidy, F. Kraus, Z. Anorg, Allg. Chem. 640 (2014) 1547–1550.
[33] Q. Niu, T.Y. Yu, J.W. Shi, et al., J. Am. Chem. Soc. 146 (2024) 20649–20659.
[34] J. Lin, G.B. Jin, L. Soderholm, Inorg. Chem. 55 (2016) 10098–10101.
[35] I. Colliard, G. Morrison, H.C.Z. Loye, M. Nyman, J. Am. Chem. Soc. 142 (2020) 9039–9047.
[36] R.E. Wilson, S. Skanthakumar, G. Sigmon, P.C. Burns, L. Soderholm, Inorg. Chem. 46 (2007) 2368–2372.
[37] N. Torapava, I. Persson, L. Eriksson, D. Lundberg, Inorg. Chem. 48 (2009) 11712–11723.
[38] T. Minato, ChemPlusChem 89 (2024) e202400402.
[39] S.T. Zheng, G.Y. Yang, Chem. Soc. Rev. 41 (2012) 7623–7646.
[40] M. Dufaye, S. Duval, T. Loiseau, CrystEngComm 22 (2020) 3549–3562.
[41] M. Fairley, D.K. Unruh, A. Donovan, S. Abeysinghe, T.Z. Forbes, Dalton Trans. 42 (2013) 13706–13714.
[42] M. Fairley, D.K. Unruh, S. Abeysinghe, T.Z. Forbes, Inorg. Chem. 51 (2012) 9491–9498.
[43] D.K. Unruh, J. de Groot, M. Fairley, et al., Inorg. Chem. 54 (2015) 1395–1404.
[44] C.H. Wang, Y. Zhang, Z. Han, et al., Chem. J. Chin. U. 46 (2025) 1–10.
[45] A. Mishra, A.J. Tasiopoulos, W. Wernsdorfer, K.A. Abboud, G. Christou, Inorg. Chem. 46 (2007) 3105–3115.
[46] X.H. Kong, Q.Y. Wu, L. Mei, et al., CCS Chem. 5 (2023) 1144–1153.
[47] J.A.S. Adams, K.A. Richardson, Econ. Geol. 55 (1960) 1653–1675.

[48] L.L. Yin, Q. Tian, X.Z. Shao, et al., Nucl. Sci. Tech. 27 (2016) 1–10.
[49] M. Wang, M. Muhammed, Nanostruct. Mater. 11 (1999) 1219–1229.
[50] X.M. Luo, Y.K. Li, X.Y. Dong, S.Q. Zang, Chem. Soc. Rev. 52 (2023) 383–444.
[51] W.H. Casey, Chem. Rev. 106 (2006) 1–16.
[52] H. Sartzi, H.N. Miras, L. Vila-Nadal, D.L. Long, L. Cronin, Angew. Chem. Int. Ed. 54 (2015) 15488–15492.
[53] C. Rocchiccioli-Deltcheff, M. Fournier, R. Franck, R. Thouvenot, Inorg. Chem. 22 (1983) 207–216.
[54] D.M.T. Eralie, T.M. Hoang, J.A. Williamson, D. Unruh, A.E.V. Gorden, Inorg. Chim. Acta 553 (2023) 121542.
[55] W.A. Deer, R.A.Howie FRS, J. Zussman, An Introduction to the Rock-Forming Minerals, Mineralogical Society of Great Britain and Ireland, London, 2013.
[56] E. Arslan, R.A. Lalancette, I. Bernal, Struct. Chem. 31 (2020) 1217–1222.
[57] Y. Zhu, Z. Wang, D. Li, et al., Angew. Chem. Int. Ed. 61 (2022) e202202853.
[58] S. Grimme, Angew. Chem. Int. Ed. 47 (2008) 3430–3434.
[59] Y.J. Liu, Q.H. Li, D.J. Li, et al., Angew. Chem. Int. Ed. 60 (2021) 4849–4854.
[60] G. Furrer, B.L. Phillips, K.U. Ulrich, R. Pothig, W.H. Casey, Science 297 (2002) 2245–2247.
[61] J.A. Howe, R.H. Loeppert, V.J. Derose, D.B. Hunter, P.M. Bertsch, Environ. Sci. Technol. 37 (2003) 4091–4097.
[62] D. Sekiguchi, S. Adachi, Opt. Mater. 42 (2015) 417–422.
[63] T. Tago, N. Kataoka, H. Tanaka, K. Kinoshita, S. Kishida, Procedia Eng. 216 (2017) 175–181.
[64] M. Bandi, V. Zade, S. Roy, et al., Cryst. Growth Des. 20 (2020) 1422–1433.
[65] X. Liu, C. Si, J. Xu, H. Sun, J. Li, Q. Han, Inorg. Chem. 64 (2025) 1263–1271.
[66] A. Sundar, S. Bhattacharya, J. Oberstein, et al., U. Kortz. Inorg. Chem. 61 (2022) 11524–11528.
[67] S. Wang, Z.X. Sun, X.Y. Zou, et al., New J. Chem. 43 (2019) 14527–14535.
[68] L. You, R. Tian, T. Zhou, R.J. Xie, Chem. Eng. J. 417 (2021) 129224.
[69] S. Abeysinghe, D.K. Unruh, T.Z. Forbes, Inorg. Chem. 52 (2013) 5991–5999.
[70] Y.J. Liu, Y.F. Sun, S.H. Shen, et al., Nat. Commun. 13 (2022) 6632.
[71] S.M. Bradley, R.A. Kydd, C.A. Fyfe, Inorg. Chem. 31 (2002) 1181–1185.
[72] S. Abeysinghe, D.K. Unruh, T.Z. Forbes, Cryst. Growth Des. 12 (2012) 2044–2051.
[73] C. Baffert, J.F. Boas, A.M. Bond, et al., Chemistry 12 (2006) 8472–8483.
[74] Y. Hamada, N. Makoni, H. Hamada, Electronic J. Biol. 12 (2016) 6–9.
[75] M. Gao, Y. Pan, Y. Jin, J. Lin, RSC Adv. 11 (2020) 760–779.
[76] W.W. Wendlandt, H.G. Hecht, Interscience publishers-J Wiley and Sons Inc. (1966) 408.
[77] A.E. Morales, E.S. Mora, U. Pal, Rev. Mex. Fis. 53 (2007) 18–22.
[78] N.B. Manson, G.A. Shah, B. Howes, C.D. Flint, Mol. Phys. 34 (2006) 1157–1174.
[79] D. Huang, H. Zhu, Z. Deng, et al., Angew. Chem. Int. Ed. 58 (2019) 3843–3847.
[80] L.A. Feigin, D.I. Svergun, Structure Analysis by Small-Angle X-Ray and Neutron Scattering, Plenum Press, New York, 1987.
[81] J. Qiu, J. Ling, A. Sui, J.E. Szymanowski, A. Simonetti, P.C. Burns, J. Am. Chem. Soc. 134 (2012) 1810–1816.